J. Fluid Mech. (2002), *vol.* 451, *pp.* 145–168.
DOI: 10.1017/S0022112001006309 Printed in the United Kingdom

Generation of slow large scales in forced rotating stratified turbulence

By LESLIE M. SMITH[1] AND FABIAN WALEFFE[2]

[1]Departments of Mathematics and Mechanical Engineering, University of Wisconsin, Madison, WI 53706, USA

[2]Departments of Mathematics and Engineering Physics, University of Wisconsin, Madison, WI 53706, USA

(Received 17 March 2001 and in revised form 3 July 2001)

Numerical simulations are used to study homogeneous, forced turbulence in three-dimensional rotating, stably stratified flow in the Boussinesq approximation, where the rotation axis and gravity are both in the $\widehat{z}$-direction. Energy is injected through a three-dimensional isotropic white-noise forcing localized at small scales. The parameter range studied corresponds to Froude numbers smaller than an $O(1)$ critical value, below which energy is transferred to scales larger than the forcing scales. The values of the ratio N/f range from $\approx 1/2$ to ∞, where N is the Brunt–Väisälä frequency and f is twice the rotation rate. For strongly stratified flows ($N/f \gg 1$), the slow large scales generated by the fast small-scale forcing consist of vertically sheared horizontal flow. Quasi-geostrophic dynamics dominate, at large scales, only when $1/2 \leqslant N/f \leqslant 2$, which is the range where resonant triad interactions cannot occur.

1. Introduction

Stratification and rotation are dominating characteristics of atmospheric and oceanic flows. Stratification and rotation lead to two distinct types of motions: fast three-dimensional small-scale inertial–gravity waves and slow quasi-geostrophic large-scale flows. Quasi-geostrophic turbulence was thus a starting point to explain, for example, the scalings of the mesoscale wind velocity spectra near the troposphere. These atmospheric spectra scale approximately as $E(k) \propto k^{-3}$ in the range 800–2500 km, and approximately as $E(k) \propto k^{-5/3}$ in the range 10–500 km (Nastrom & Gage 1985). Charney (1971) related quasi-geostrophic turbulence to the two-dimensional forward enstrophy cascade range with energy spectrum $E(k) \propto k^{-3}$ (Kraichnan 1967). Lilly (1983) reasoned that initially three-dimensional isotropic turbulence subjected to strong stratification would separate into gravity waves and quasi-two-dimensional turbulence within horizontal layers; a two-dimensional inverse cascade within layers, fed by convective instability (e.g. Vincent & Schlatter 1979), could then possibly explain the observed $k^{-5/3}$ scaling of the atmospheric spectra in the range 10–500 km (Nastrom & Gage 1985). Gage & Nastrom (1986) suggested wave breaking as the source of energy for the quasi-two-dimensional inverse cascade. Lilly (1989) predicted, and Maltrud & Vallis (1991) demonstrated numerically, that a forward cascade of enstrophy with $E(k) \propto k^{-3}$, fed by large-scale instability, and an inverse cascade of energy with $E(k) \propto k^{-5/3}$, fed by small-scale instability, can coexist without significant distortion. In this work, as in our previous studies (Smith & Waleffe 1999), we start from fully three-dimensional flow, and investigate the

possibility of energy transfer to large scales, including the scalings of energy spectra, the development of structures, and transfer mechanisms.

In Smith, Chasnov & Waleffe (1996), we considered turbulence in small-aspect-ratio domains, where the largest horizontal scale L is much greater than the largest vertical scale H. Numerical simulations with two-dimensional forcing at scales $> H$ showed that the two-dimensional inverse cascade of energy is stable to three-dimensional small-scale fluctuations. The two-dimensional isotropic inverse cascade with energy spectrum $E(k) \propto k^{-5/3}$ is also stable to two-dimensional forcing at scales $< H$ when the flow is subjected to sufficiently fast rotation. In Smith & Waleffe (1999), simulations of rotating turbulence, now with isotropic, three-dimensional, random forcing at small scales in unit-aspect-ratio domains ($L = H$), revealed that backward energy transfer can occur in fully three-dimensional rotating turbulence but its nature is different from the two-dimensional isotropic inverse cascade. First, the transfer of energy from small to large scales in three-dimensional rotating flow is anisotropic; only vertically independent horizontal motions are populated for wavenumbers smaller than the forcing wavenumbers. Second, population of modes in the horizontal plane corresponds to the formation of large-scale cyclonic vortical columns. This is in contrast to the isotropic energy transfer to large scales observed in two-dimensional turbulence, in which case only finite-size effects lead to the formation of large-scale structures (e.g. Smith & Yakhot 1994; Paret & Tabeling 1998). Third, the large-scale energy spectrum appears to approach the scaling $E(k) \propto k^{-3}$. The presence of anisotropic dispersive waves significantly influences the large-scale dynamics of rotating flow. With forcing at small scales, the effects of anisotropy are even more pronounced than in decaying rotating turbulence (see Cambon 2001 and references therein).

All fundamental models for geophysical flows involve the complex interaction between dispersive waves and turbulence, e.g. the β-plane model, the three-dimensional Navier–Stokes equations in a rotating frame, the two-dimensional and three-dimensional Boussinesq equations for rotating stably stratified flow. Similar to the results of Smith & Waleffe (1999), simulations of forced β-plane turbulence (Smith & Waleffe 1999; Chekhlov *et al.* 1996), forced two-dimensional stratified turbulence (Smith 2001), and forced two-dimensional turbulence on a sphere (Huang, Galperin & Sukoriansky 2000) show that, for strong rotation or stratification, energy is transferred to large scales, and accumulates on the slow manifold. In each of these cases, the slow manifold follows from the dispersion relation by choosing the wavevector such that the ratio of the wave frequency to the system frequency tends to zero, where the system frequency is either the rotation rate, buoyancy frequency or inverse-time scale βk_β, with k_β proportional to the Rossby deformation radius. Since the dispersion relations for these flows are anisotropic, the large-scale motions are also anisotropic. They correspond either to one-dimensional shear flows (in two-dimensional β-plane and two-dimensional stratified flows) or two-dimensional flows (in three-dimensional rotating flows).

The situation is more complex in three-dimensional stratified flow where there are two kinds of zero-frequency modes: the vertically sheared horizontal flows (VSHF) with $k_h \equiv (k_x^2 + k_y^2)^{1/2} = 0$, and the potential vorticity (PV) modes that exist for every wavevector $\boldsymbol{k}$. The VSHF modes again correspond to zero wave frequency in the dispersion relation, where the dispersion relation is given by $\sigma^{\pm}(\boldsymbol{k}) = \pm N k_h/k$ with $k = |\boldsymbol{k}|$. For purely stratified flow at small Froude number ($Fr \approx 0.2$) forced randomly at small scales, we find anisotropic transfer of energy to the VSHF modes. Previous numerical calculations of forced (Herring & Metais 1989) and decaying stratified

turbulence (see e.g. Staquet & Godeferd 1998) have shown horizontal layering, but none have exhibited the large accumulation of energy at large scales captured by our forced simulations over long integration times. Herring & Metais (1989) used a two-dimensional forcing with resolution 64^3, whereas we use a three-dimensional, isotropic forcing with resolution 128^3. An anisotropic statistical model of decaying stratified turbulence (Godeferd & Cambon 1994) also shows energy concentration toward the VSHF modes. That study indicates that the PV modes play a dominant role, in decay, for the relative concentration toward the VSHF, while in our forced simulations the inertial–gravity waves create the VSHF (§ 5). Those results are not inconsistent; rather they underline the significant differences between long-time simulations with small-scale isotropic forcing and short-time simulations of decay from large-scale isotropic initial conditions. The reader is referred to the recent review by Riley & Lelong (2000) for further discussion and references on stably stratified flows.

In rotating, stably stratified flow, the geostrophic motions are the only modes with zero frequency. We find that they dominate at large scales when the ratio of stratification to rotation, as measured by N/f, where N is the Brunt–Väisälä frequency and f is twice the rotation rate, is in the range $1/2 \leqslant N/f \leqslant 2$ for small values of the Froude number, specifically $Fr \approx 0.21$. Interestingly, this is also the N/f range where three-wave resonant interactions cannot occur. For these values of Fr and N/f, large-scale energy spectra are closer to power-law scaling with $E(k) \propto k^{-5/3}$, consistent with previous calculations (Metais *et al.* 1996). However for $N/f \gg 1$, our simulations show that the dominant large-scale motions are vertically sheared, horizontal flows as in purely stratified flow, corresponding to modes with small but non-zero frequency $\sigma = \pm f$ and horizontal wavenumber $k_h = 0$. This result may be relevant to some atmospheric dynamics where the stratificiation is much stronger than rotation. For the opposite limit of strong rotation with weak stratification (Rossby number $Ro < 1$, $N/f \ll 1$) we recover our previous results where the flow is dominated at large scales by cyclonic vortices and the energy spectrum scales approximately like $E(k) \propto k^{-3}$ (Smith & Waleffe 1999).

A common result of Chekhlov *et al.* (1996), Smith & Waleffe (1999), Smith (2001), Huang *et al.* (2000) and the present work is the universality of energy transfer to large-scale slow modes when the Rossby, Froude or Rhines number is smaller than an $O(1)$ critical value. This result is surprising given that resonant triad interactions cannot transfer energy from fast waves directly to slow modes with zero frequency, at first order in a weakly nonlinear expansion in ϵ, where ϵ is the relevant small parameter (i.e. the Rossby, Froude or Rhines number). This decoupling between fast and slow modes for resonant triad interactions has been shown for a broad variety of flows, namely for rotating flows (Greenspan 1969), β-plane flows (Longuet-Higgins & Gill 1967), stratified flows (Phillips 1968; Lelong & Riley 1991), rotating stratified flows (Bartello 1995; Embid & Madja 1998, Majda & Embid 1998), as well as for rotating shallow-water flows (Warn 1986; Embid & Majda 1996). Asymptotically speaking, these analyses are valid up to time scales of order $1/\epsilon$, with wave oscillations occurring on the fast $O(1)$ time scale. Our computations pertain to the much longer time scale $1/\epsilon^2$. We emphasize however that these asymptotic arguments only serve as guides for our thinking because ϵ is fixed and not very small in our computations ($\epsilon \approx 0.1$). In fact, there seems to be a well-defined critical $\epsilon_c = O(1)$ above which we see a three-dimensional cascade to small scales but below which there is transfer of energy to large scales, after long times, with generation of substantial anisotropy in most cases. We believe that this effect is important for models of long-term change in atmospheric dynamics, ocean circulation and climate.

The equations for rotating stratified flows are given in § 2, along with the eigenmodes of the linearized equations that are the basis for the numerical calculations. Section 3 gives parameter definitions and describes the details of the numerical simulations. The numerical results are presented in §§ 4 and 5: for stratified flows with varying Froude number (§ 4), and rotating, stratified flows with varying ratio of Rossby to Froude number, i.e. varying values of N/f (§ 5). In all cases, we demonstrate the nonlinear transfer of energy from fast small-scale fluctuations to slow large-scale motions corresponding to eigenmodes of the linearized equations with zero or near-zero frequency. We also report on a few decay experiments at the end of § 5. A general discussion and interpretation of the results are given in § 6.

2. Governing equations and linear eigenmodes

The Boussinesq equations for vertically stratified flow rotating about the vertical $\widehat{\boldsymbol{z}}$-axis, in dimensional form, are (e.g. Salmon 1998)

$$\frac{\mathrm{D}\boldsymbol{v}}{\mathrm{D}t} + f\widehat{\boldsymbol{z}} \times \boldsymbol{v} + N\theta\widehat{\boldsymbol{z}} + \nabla P = \nu_o \nabla^2 \boldsymbol{v} + \boldsymbol{f}_u, \tag{2.1}$$

$$\frac{\mathrm{D}\theta}{\mathrm{D}t} - N(\boldsymbol{v} \cdot \widehat{\boldsymbol{z}}) = \kappa \nabla^2 \theta, \tag{2.2}$$

$$\nabla \cdot \boldsymbol{v} = 0, \tag{2.3}$$

where $\boldsymbol{v}$ is the Eulerian velocity, f is twice the frame rotation rate, P is the effective pressure, N the buoyancy frequency, $\mathrm{D}/\mathrm{D}t = \partial/\partial t + \boldsymbol{v} \cdot \nabla$ is the material derivative, ν_o is the kinematic viscosity, κ is the diffusion coefficient and θ, which has units of velocity, is proportional to the density fluctuations. The total mass density ρ has been decomposed as

$$\rho = \rho_o - bz + \rho', \quad \rho' = \left(\frac{b\rho_o}{g}\right)^{1/2} \theta, \tag{2.4}$$

where ρ_o is a reference density, b is a positive constant (for uniform stable stratification), z is the vertical coordinate and g is the gravitational acceleration. The buoyancy (Brunt–Väisälä) frequency N is

$$N = \left(\frac{gb}{\rho_o}\right)^{1/2}. \tag{2.5}$$

The term $\boldsymbol{f}_u$ in (2.1) represents external forcing of the velocity; note that we do not consider external forcing of the density fluctuations θ.

In the inviscid, unforced limit ($\nu_0 = \kappa = \boldsymbol{f}_u = 0$), the Boussinesq equations (2.1)–(2.3) conserve potential vorticity, $\boldsymbol{\omega}_a \cdot \nabla\rho$:

$$\frac{\mathrm{D}}{\mathrm{D}t}(\boldsymbol{\omega}_a \cdot \nabla\rho) = 0, \tag{2.6}$$

where $\boldsymbol{\omega}_a = \boldsymbol{\omega} + f\widehat{\boldsymbol{z}}$ is the absolute vorticity and $\boldsymbol{\omega} = \nabla \times \boldsymbol{v}$ is the vorticity. Conservation of potential vorticity following fluid particles, in the Boussinesq approximaion, is equivalent to conservation of the volume of a fluid element because $\boldsymbol{\omega}_a$ evolves as a line element and $\nabla\rho$ as a surface element. The potential vorticity can be expressed in terms of $\boldsymbol{\omega}$ and θ. Using (2.4) and (2.5) yields

$$\boldsymbol{\omega}_a \cdot \nabla\rho = \left(\frac{b\rho_o}{g}\right)^{1/2} (-Nf + f\widehat{\boldsymbol{z}} \cdot \nabla\theta - N\widehat{\boldsymbol{z}} \cdot \boldsymbol{\omega} + \boldsymbol{\omega} \cdot \nabla\theta) \tag{2.7}$$

and PV conservation (2.6) can be rewritten as

$$\left(\frac{\partial}{\partial t}+\boldsymbol{v}\cdot\nabla\right)(f\widehat{\boldsymbol{z}}\cdot\nabla\theta-N\widehat{\boldsymbol{z}}\cdot\boldsymbol{\omega}+\boldsymbol{\omega}\cdot\nabla\theta)=0. \tag{2.8}$$

In the following, 'potential vorticity' refers to the quantity $PV\equiv f\widehat{\boldsymbol{z}}\cdot\nabla\theta-N\widehat{\boldsymbol{z}}\cdot\boldsymbol{\omega}+\boldsymbol{\omega}\cdot\nabla\theta$.

Conservation of potential vorticity is an important constraint on the dynamics leading, in particular, to two distinct classes of linear eigenmodes: inertial–gravity waves with non-zero frequency and zero potential vorticity, and PV modes with zero frequency and non-zero potential vorticity. For an unbounded or periodic domain, the linear eigenmodes of (2.1)–(2.3) are Fourier modes

$$\begin{pmatrix}\boldsymbol{v}\\ \theta\end{pmatrix}(\boldsymbol{x},t)=\boldsymbol{\phi}(\boldsymbol{k})\mathrm{e}^{\mathrm{i}(\boldsymbol{k}\cdot\boldsymbol{x}-\sigma(\boldsymbol{k})t)}, \tag{2.9}$$

where $\boldsymbol{\phi}=(\widehat{\boldsymbol{v}},\hat{\theta})$. There are only three modes per wavevector as a result of the continuity constraint (2.3). In general, two of these modes $\boldsymbol{\phi}^{\pm}$ have non-zero frequency $\sigma^{\pm}$ and the third $\boldsymbol{\phi}^{0}$ has zero frequency $\sigma^{0}=0$. The latter corresponds to a PV mode, while the former are inertial–gravity waves with no PV. Indeed in the linear limit, PV conservation (2.8) reduces to

$$\frac{\partial}{\partial t}\left(f\widehat{\boldsymbol{z}}\cdot\nabla\theta-N\widehat{\boldsymbol{z}}\cdot\boldsymbol{\omega}\right)=0, \tag{2.10}$$

or $\sigma(\mathrm{i}fk_z\hat{\theta}-N\hat{\omega}_z)=0$ in Fourier space. This requires $\sigma=0$ for PV modes or $\mathrm{i}fk_z\hat{\theta}-N\hat{\omega}_z=0$ (i.e. no linear PV) for wave modes.

Substituting (2.9) into the linearized form of equations (2.1)–(2.3) leads to the dispersion relation for the inertial–gravity waves

$$\sigma^{\pm}(\boldsymbol{k})=\pm\frac{(N^2k_h^2+f^2k_z^2)^{1/2}}{k}, \tag{2.11}$$

where $k_h=\left(k_x^2+k_y^2\right)^{1/2}$. The eigenfunction $\boldsymbol{\phi}^{+}$ corresponding to σ^{+} in (2.11) is

$$\boldsymbol{\phi}^{+}=\frac{1}{\sqrt{2}\,\sigma k}\left(\frac{k_z}{k_h}\left(\sigma k_x+\mathrm{i}k_yf\right),\frac{k_z}{k_h}\left(\sigma k_y-\mathrm{i}k_xf\right),-\sigma k_h,-\mathrm{i}Nk_h\right), \tag{2.12}$$

where $\sigma=|\sigma^{\pm}(\boldsymbol{k})|$. The eigenfunction $\boldsymbol{\phi}^{-}$ corresponding to σ^{-} in (2.11) is the complex conjugate of $\boldsymbol{\phi}^{+}$. The PV mode $\boldsymbol{\phi}^{0}$, which has zero frequency ($\sigma^{0}=0$), is

$$\boldsymbol{\phi}^{0}=\frac{1}{\sigma k}\left(Nk_y,-Nk_x,0,fk_z\right). \tag{2.13}$$

Its contribution to the linear part of the PV (2.10) has the simple form $\mathrm{i}fk_z\hat{\theta}-N\hat{\omega}_z=\mathrm{i}\sigma k=\mathrm{i}(N^2k_h^2+f^2k_z^2)^{1/2}$.

Two special cases must be considered: (i) $k_h=0$ and (ii) $k_z=N=0$. For case (i), when the wavevector is parallel to the rotation and stratification axis, orthonormal eigenfunctions satisfying continuity are

$$\boldsymbol{\phi}^{+}=\left(\frac{1+\mathrm{i}}{2},\frac{1-\mathrm{i}}{2},0,0\right),\quad \boldsymbol{\phi}^{-}=\overline{\boldsymbol{\phi}^{+}},\quad \boldsymbol{\phi}^{0}=(0,0,0,1), \tag{2.14}$$

where the overline denotes complex conjugate. These are the vertically sheared horizontal flow modes or *VSHF modes*. They have no vertical vorticity and no potential

vorticity. They also have no vertical velocity because of the continuity constraint (2.3). The wave frequencies corresponding to $\boldsymbol{\phi}^+$ and $\boldsymbol{\phi}^-$ are, respectively, $\sigma^+ = f$ and $\sigma^- = -f$. Density fluctuations represented by $\boldsymbol{\phi}^0$ have zero frequency, $\sigma^0 = 0$. Special case (ii), $k_z = N = 0$, corresponds to pure rotation with wavevector perpendicular to the rotation axis. In this case, the eigenmodes are all slow (geostrophic) modes with zero frequency $\sigma^+ = \sigma^- = \sigma^0 = 0$, taken as

$$\boldsymbol{\phi}^+ = \frac{1}{\sqrt{2}\,k_h}(\mathrm{i}k_y, -\mathrm{i}k_x, -k_h, 0), \quad \boldsymbol{\phi}^- = \overline{\boldsymbol{\phi}^+}, \quad \boldsymbol{\phi}^0 = (0,0,0,1). \tag{2.15}$$

In the (numerical) solution and analysis procedure, we expand the Fourier-transformed velocity and density fluctuations in terms of the orthonormal, solenoidal eigenmodes

$$\begin{pmatrix} \widehat{\boldsymbol{v}} \\ \widehat{\theta} \end{pmatrix}(\boldsymbol{k},t) = a^+(\boldsymbol{k},t)\,\boldsymbol{\phi}^+(\boldsymbol{k}) + a^-(\boldsymbol{k},t)\,\boldsymbol{\phi}^-(\boldsymbol{k}) + a^0(\boldsymbol{k},t)\,\boldsymbol{\phi}^0(\boldsymbol{k}), \tag{2.16}$$

$$a^{(\alpha)}(\boldsymbol{k},t) = \overline{\boldsymbol{\phi}^{(\alpha)}} \cdot \begin{pmatrix} \widehat{\boldsymbol{v}} \\ \widehat{\theta} \end{pmatrix} \tag{2.17}$$

where $\alpha = -, 0, +$. In the inviscid, unforced case ($\nu_0 = \kappa = \boldsymbol{f}_u = 0$), the evolution of $a^\alpha \exp(\mathrm{i}\sigma^{(\alpha)}t)$ results from nonlinear interactions only

$$\frac{\mathrm{d}}{\mathrm{d}t}(a^\alpha \exp \mathrm{i}\sigma^\alpha t) = -\overline{\boldsymbol{\phi}^\alpha} \cdot \begin{pmatrix} \widehat{\boldsymbol{v}\cdot\nabla\boldsymbol{v}} \\ \widehat{\boldsymbol{v}\cdot\nabla\theta} \end{pmatrix} \exp(\mathrm{i}\sigma^\alpha t), \tag{2.18}$$

where $\widehat{\boldsymbol{v}\cdot\nabla\boldsymbol{v}}$ and $\widehat{\boldsymbol{v}\cdot\nabla\theta}$ are the Fourier transforms of the nonlinear terms. Note that with these eigenmode definitions, reality of the underlying fields, which requires $\boldsymbol{u}(\boldsymbol{k}) = \overline{\boldsymbol{u}}(-\boldsymbol{k})$, does not imply $a^\alpha(\boldsymbol{k}) = \overline{a^\alpha}(-\boldsymbol{k})$ for the modal amplitudes. For the PV modes (2.13) for instance, reality implies $a^0(\boldsymbol{k}) = -\overline{a^0}(-\boldsymbol{k})$.

3. The numerical simulations

Equations (2.1)–(2.3) are solved using a pseudo-spectral code in a triply periodic cube of resolution 128^3 Fourier modes. The linear terms are treated using an integrating factor technique, in effect removing them from the time integration (as in (2.18) above). The viscous term is treated with an integrating factor as well (Rogallo 1981). At each step of the third-order Runge–Kutta time-stepping scheme, the Fourier-transformed velocity and density fields are projected onto the eigenmodes (2.16), and each mode is multiplied by the proper time-integration factor. The time step is chosen to sufficiently resolve the wave oscillations (i.e. $\sigma\Delta t < (N+f)\Delta t < 0.2$). The projection onto the inertial–gravity modes automatically satisfies the incompressibility constraint and eliminates pressure. The nonlinear terms $\boldsymbol{v}\cdot\nabla\boldsymbol{v}$ and $\boldsymbol{v}\cdot\nabla\theta$ are calculated in physical space and fast Fourier transforms (FFTs) are used to go back and forth between Fourier and physical space. The simulations were performed on Silicon Graphics multi-processor computers, which provide compiler parallelization and optimized, parallelized FFTs. The code runs at 36 s per time step on four SGI 12K 270 MHz processors (a local SGI Origin200). Our longest run was for $N/f = 100$, which was integrated for 62 600 time steps, and thus required about twenty-six days of computer time.

The forcing spectrum $F(k)$ is Gaussian with standard deviation $s = 1$ and energy

input rate $\epsilon_f = 1$, given by

$$F(k) = \epsilon_f \frac{\exp(-0.5(k-k_f)^2/s^2)}{(2\pi)^{1/2}s}. \tag{3.1}$$

Based on the energy input rate ϵ_f and the peak wavenumber k_f of the force, we define the Froude and Rossby numbers as

$$Fr = \frac{(\epsilon_f k_f^2)^{1/3}}{N}, \quad Ro = \frac{(\epsilon_f k_f^2)^{1/3}}{f}. \tag{3.2}$$

For the runs presented in § 4 ($f = 0$), we vary N and k_f to vary the Froude number, and in § 5, we fix $N = 40$ and $k_f = 24$ such that the Froude number is $Fr = 0.21$ and vary the Rossby number. Note that $N/f = Ro/Fr$.

The dissipation of the velocity at small scales is modelled by a hyperviscosity term

$$(-1)^{p+1}\nu(\nabla^2)^p \boldsymbol{v} \tag{3.3}$$

(with $p = 8$ unless otherwise specified) in place of the normal viscosity term $\nu\nabla^2\boldsymbol{v}$. Likewise the dissipation of the density fluctuations is modelled by $(-1)^{p+1}\kappa(\nabla^2)^p\theta$. The purpose of using hyperviscosity, which turns on much more abruptly than the gradual increase of normal viscosity at small scales, is to eliminate as much as possible the effects of viscosity at intermediate scales, thus extending the turbulence inertial ranges. Following Chasnov (1994), the hyperviscosity is taken to be

$$\nu \equiv 2.5\left(\frac{E(k_m,t)}{k_m}\right)^{1/2} k_m^{2-2p} \tag{3.4}$$

where k_m is the highest available wavenumber and $E(k_m, t)$ is the kinetic energy in the highest available wavenumber shell. A similar expression is used for the hyperdissipation, using the energy of the density fluctuations in the highest available wavenumber shell. By using random forcing and hyperviscosity at small scales, we in effect assume a Langevin-type model for the small-scale dynamics, as in idealized climate models (Hasselman 1976; Majda, Timofeyev & Vanden Eijnden 1999). The large-scale dynamics are then fully resolved. In order to study the nonlinear interactions between waves in isolation from other effects, we consider periodic flows, thereby eliminating viscous boundary layers. Although the atmosphere is periodic in the horizontal directions, there are some periodic large-scale flows that will be excluded by, for example, ocean boundaries. All simulations are dealiased using the 2/3 rule (see e.g. Canuto *et al.* 1988).

4. Stratified turbulence ($f = 0,\ N \neq 0$)

For purely stratified turbulence, we begin by comparing kinetic energy† vs. time for three values of the Froude number, $Fr = 0.42$, 0.28 and 0.21 (figure 1). Three of the four runs shown in figure 1 have peak forcing at $k_f = 24$ (solid curves), and one has $k_f = 20$ ($Fr = 0.21$, dashed curve). For $Fr = 0.42$, after a short period of initial growth, the kinetic energy does not grow in time for nonlinear times up to $T \equiv t(\epsilon_f k_f^2)^{1/3} \approx 800$; all of the energy input by the random force is dissipated at small scales by viscosity, and there is no transfer of energy to scales larger than the

† Unconventially, we define the 'kinetic energy' as the volume average of $|\boldsymbol{v}|^2/2$. Likewise, the (available) 'potential energy' is the volume average of $\theta^2/2$.

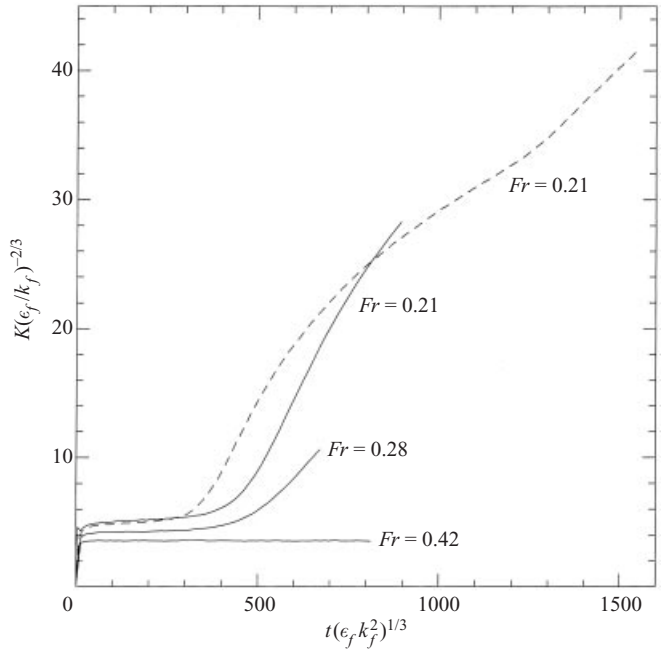

FIGURE 1. Kinetic energy vs. time ($f = 0$). The solid curves have peak forcing wavenumber $k_f = 24$ and the dashed curve has peak wavenumber $k_f = 20$.

forcing scales. For the other runs with $Fr = 0.28$ and 0.21, there is strong growth of the kinetic energy after several hundred nonlinear times, indicating transfer of energy to scales larger than the forcing scales. Thus there is a critical value of the Froude number below which energy is transferred simultaneously to large and small scales, similar to the case of purely rotating turbulence in which there is a critical Rossby number for the transfer of energy to large scales (Smith & Waleffe 1999). For these moderate values of the Froude number $Fr = O(10^{-1})$, the difference between the energy input rate and the energy dissipation rate, denoted $\epsilon^<$, increases as the Froude number decreases below that critical value.

Figure 2 shows spectra for the run with $Fr = 0.21$ and $k_f = 24$, at the latest time ($T \approx 900$ in figure 1). The spectrum $E(k)$ of the total kinetic energy is given by the solid line, and the spectrum of kinetic energy in the VSHF modes (with $k_h = 0$) is given by the dashed line. Recall that the VSHF modes have kinetic energy only. One sees a pile-up of energy, especially in wavenumbers $k_z = 9$ and 11, where all of the energy is in the VSHF modes, corresponding to vertically sheared, horizontal layers. The energy spectrum of the (unforced) density fluctuations is shown in figure 2 by the dash-dot line; there is clearly a weaker transfer of potential energy to scales larger than the forcing scale. The transfer of potential energy to larger scales must be the result of inertial–gravity wave interactions because the PV modes (2.13) have zero scalar component when $f = 0$. In this way the scalar transfer is a diagnostic, suggesting that wave interactions are responsible for the transfer of energy to larger scales. A simulation for $N/f = 100$ with the PV modes artificially suppressed indicates that the PV modes do indeed inhibit the transfer of energy to large scales by the waves for large N/f (see § 5). Figure 3 shows spectra for the run with $Fr = 0.21$ and $k_f = 20$, at the latest time of the run ($T \approx 1500$ in figure 1). As for $k_f = 24$, all of

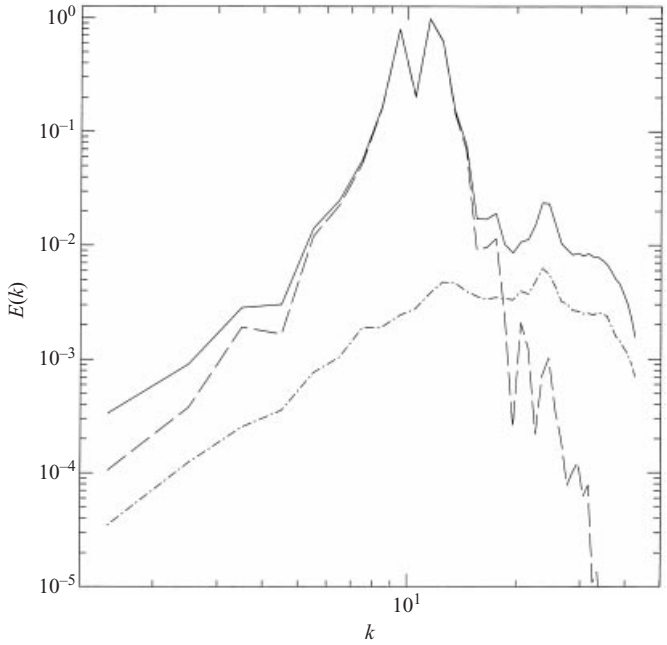

FIGURE 2. Kinetic energy (solid) vs. wavenumber for $Fr = 0.21$ ($f = 0$) with peak forcing wavenumber $k_f = 24$ ($T \approx 900$). The dashed line is energy in the VSHF modes (2.14), and the dash-dot line is the potential energy in the density fluctuations.

the large-scale kinetic energy is in the VSHF modes (dashes), and now the pile-up of energy is most pronounced for wavenumbers $k_z = 7$ and 9.

The pile-up of energy in selected small wavenumbers is clearly a long-time effect, noticeable only after several hundred nonlinear time scales. This is probably the main reason why it has not been previously observed. The wavenumber selection and lack of power-law scaling appears to be related to the PV modes and perhaps also to the low resolution. The simulation for $N/f = 100$ with PV modes suppressed shows earlier growth of energy and spectra with less wavenumber selectivity (figures 4 and 8). Simulations of forced two-dimensional stratified turbulence at resolution 512^2, where PV modes do not exist, also show energy accumulation in the VSHF without wavenumber selectivity (Smith 2001).

5. Rotating stratified turbulence ($f \neq 0,\ N \neq 0$)

5.1. *Forced for* $H/L = 1$

Kinetic energy vs. time for Froude number $Fr = 0.21$ and varying values of the Rossby number $Ro = 21, 2.1, 0.42, 0.21$ and 0.10 is shown in figure 4. Here the peak forcing wavenumber k_f is fixed at $k_f = 24$. The run with $Fr = 0.21$ and $Ro = 21$ ($N/f = 100$), relevant to atmospheric mesoscales, was integrated to $T \equiv t(\epsilon_f k_f^2)^{1/3} \approx 2200$, which is off the scale of figure 4. In all cases, energy is transferred to scales larger than the forcing scales, but the transfer process is much slower for times $T < 400$ for $N/f = 100$ and 10 than it is for the smaller ratios $1/2 \leqslant N/f \leqslant 2$. The strong growth of kinetic energy after $T \approx 400$ for large ratios $N/f = 100$ and 10 corresponds to pile-up of the total energy $E_T(k)$ (kinetic and potential) in VSHF (near-zero) modes with $k_h = 0$ and frequency $\sigma^{\pm} = \pm f \ll N$. As in the case of purely stratified

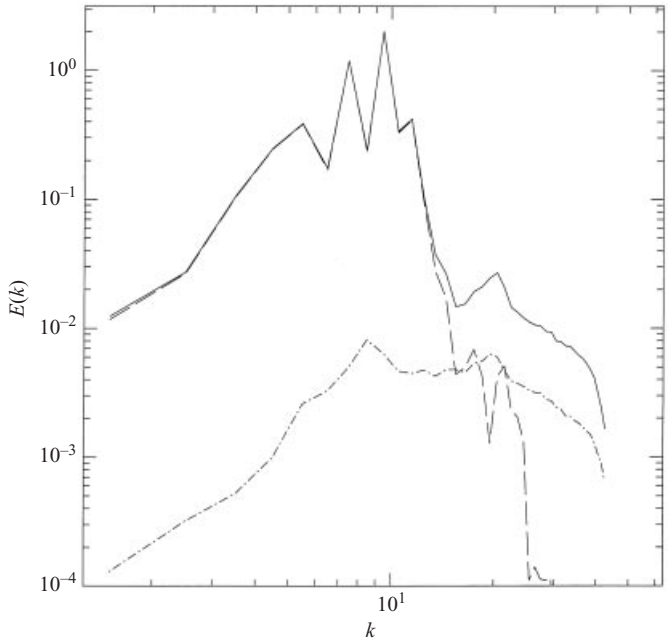

FIGURE 3. Kinetic energy (solid) vs. wavenumber for $Fr = 0.21$ ($f = 0$) with peak forcing wavenumber $k_f = 20$ ($T \approx 1500$). The dashed line is energy in the VSHF modes (2.14), and the dash-dot line is the energy of density fluctuations.

turbulence, the pile-up occurs in selected wavenumbers k_z smaller than the forcing wavenumbers (figures 5 and 9). For $N/f = 100$, after 2200 nonlinear times, the most energetic wavenumbers are $5 \leqslant k_z \leqslant 12$, with peaks remaining at $k_z = 5$, 8, 11 and 12. For even longer times, it is not clear how the energy spectrum of these large-scale modes will evolve, but there is no indication of power-law scaling for these times $T < 2200$. The rate of energy input $\epsilon^<$ to large scales appears to approach a constant value of $\epsilon^</\epsilon_f \approx 0.025$ (see figure 6), i.e. the energy input to large scales is only about 2.5% of the total energy input. Using the data of Vincent & Schlatter (1979), Smith & Yakhot (1994) estimated that on the order of 5% of the energy generated in cumulus clouds is transported to the synoptic scales, consistent with the present simulations at large N/f. The physical-space velocity field consists of vertically sheared, horizontal layers with spacing between $2\pi/5 = 1.26$ and $2\pi/12 = 0.52$ (figure 7).

In order to investigate the role of the PV modes in the dynamics for large N/f, we ran a simulation for $Fr = 0.2$ and $N/f = 100$, where the forcing remained the same but the PV modes were artificially removed at each time step (i.e. $a^0 = 0$ in (2.16)). The suppression of the PV modes effectively reduces the energy input rate ϵ_f by 1/3 and therefore the Froude and Rossby numbers (3.2) by 13%. Nonetheless, the energy grows earlier and faster when the PV modes are suppressed (curve with triangles in figure 4). Spectra at time $T \approx 1608$ are shown in figure 8, which should be compared to figure 5. The spectra of the no-PV simulation also show the strong energy concentration in the VSHF but they do not show the wavenumber selectivity seen in the full simulations. It is not impossible that the spectra may in fact be building toward $E(k) \propto k^{-3}$ scaling, analogous to forced rotating flow (Smith & Waleffe 1999). The spectra also show significantly more available potential energy at

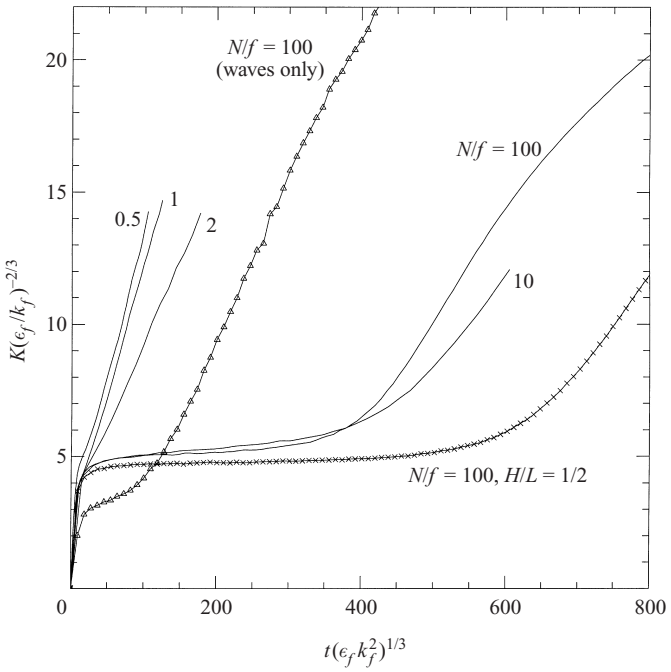

FIGURE 4. Kinetic energy vs. time for $Fr = 0.21$ and varying values of N/f.

the largest scales. Based on this simulation, it seems clear that the PV modes inhibit the transfer of energy to large scales of the VSHF by the wave modes for large N/f.

As can be seen in figure 9, for $N/f = 10$ at $T = 605$, the VSHF modes dominate for $11 \leqslant k_z \leqslant 15$. The physical-space velocity field consists of horizontal layers with rough spacing of about $l \approx 0.5$. The PV modes are seen to dominate at smaller wavenumbers $k < 8$, but with energy an order of magnitude smaller than the energy of the VSHF modes with $11 \leqslant k_z \leqslant 15$. At this value of $N/f = 10$, there is a competition at large scales between the near-zero VSHF modes and the exactly zero PV modes.

With Froude number $Fr = 0.21$ and moderate values of the Rossby number $0.10 \leqslant Ro \leqslant 0.42$, energy is transferred from the forced modes to the large-scale PV modes. Figure 10(*a–c*) shows, respectively, energy spectra for $Ro = 0.42$, 0.21 and 0.10. One sees that in all three cases, the total energy (solid) and the energy in the PV modes (long dashes) coincide for scales larger than the forcing scale. All spectra, including the spectrum of kinetic energy (short dashes) and the spectrum of density fluctuations (dash-dot), are closer to power-law behaviour than the spectra for large values of N/f, and one could speculate that the scaling $k^{-5/3}$ would be confirmed by higher resolution data.

Since there are no resonant triad interactions in the range $1/2 \leqslant N/f \leqslant 2$, as shown in the discussion section, the latter do not play a role in energy transfer to large scales in this parameter range where the dominant large scales are the geostrophic motions. Figure 11 shows spectra from a simulation of forced quasi-geostrophic turbulence, where the forcing is identical but the waves are artificially removed at each time step (i.e. $a^{\pm} = 0$ in (2.16)), with $Fr = 0.21$, $N/f = 2$ and $T \approx 110$. The spectra are very similar to spectra for the full simulation (figure 10*a*). However, it takes less time for energy to reach the box size when the waves are removed. The waves thus

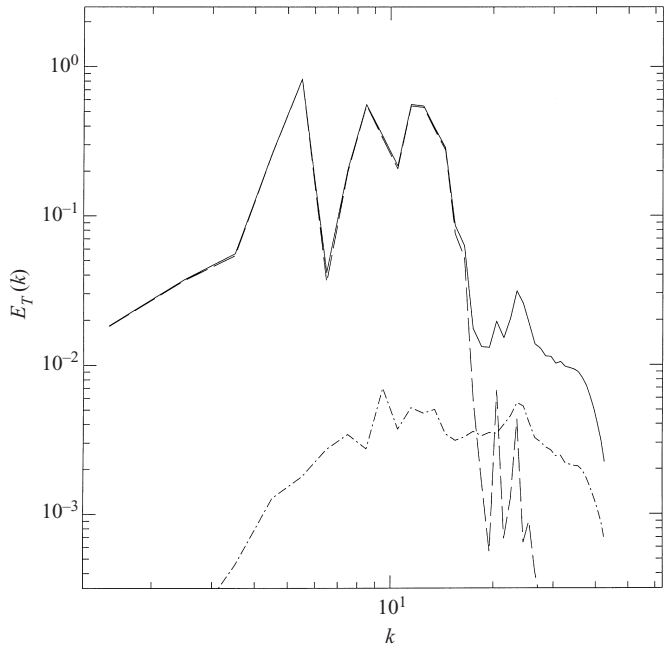

FIGURE 5. Total energy vs. wavenumber (solid) for $Fr = 0.21$, $Ro = 21$ ($N/f = 100$) and $T \approx 2200$; total energy in the VSHF modes (2.14) with $\sigma^{\pm} = \pm f$ (long dashes); potential energy of the density fluctuations (dash-dot).

appear to reduce slightly the efficiency of the quasi-geostrophic inverse energy cascade. Similar results were found for forced quasi-geostrophic turbulence with $Fr = 0.21$ and $N/f = 1, 2$.

With the Froude number fixed at $Fr = 0.21$ and decreasing N/f ($N/f = 2$, 1 and $1/2$), the physical-space fields show an increased tendency towards the development of vortical columns. Two contour levels of the zonal velocity for the run with $Fr = 0.21$ and $N/f = 2$ ($Ro = 0.42$) are shown in figure 12(a), where one sees a fully three-dimensional structure, perhaps with tendency towards a layered structure. Figure 12(b) shows two contour levels of the zonal velocity for the run with $Fr = 0.21$ and $N/f = 1/2$ ($Ro = 0.1$). In contrast to figure 12(a), one sees in figure 12(b) a tendency towards vortical columns with some vertical structure (some dependence on the vertical wavenumber k_z). The same result is found for forced quasi-geostrophic turbulence, where only the PV modes are kept. Thus, for fixed $Fr = 0.21$, there is a smooth transition from vertically sheared, horizontal layers to vortical columns as the Rossby number is decreased. For the case of pure rotation at the same Rossby number $Ro = 0.1$ (Smith & Waleffe 1999), there is transfer of energy from the forced modes to large-scale modes with $k_z = 0$, corresponding to large-scale cyclonic vortical columns.

5.2. *Forced for* $H/L = 1/2$

Since horizontal length scales are greater than vertical length scales in most geophysical flows, it is natural to ask how the results vary with aspect ratio H/L. We have already discussed one problem associated with small-aspect-ratio simulations and finite resolution, namely the severe restriction of resonant triads: sparsity of wavenumbers inhibits resonant transfer. In purely rotating turbulence forced in the

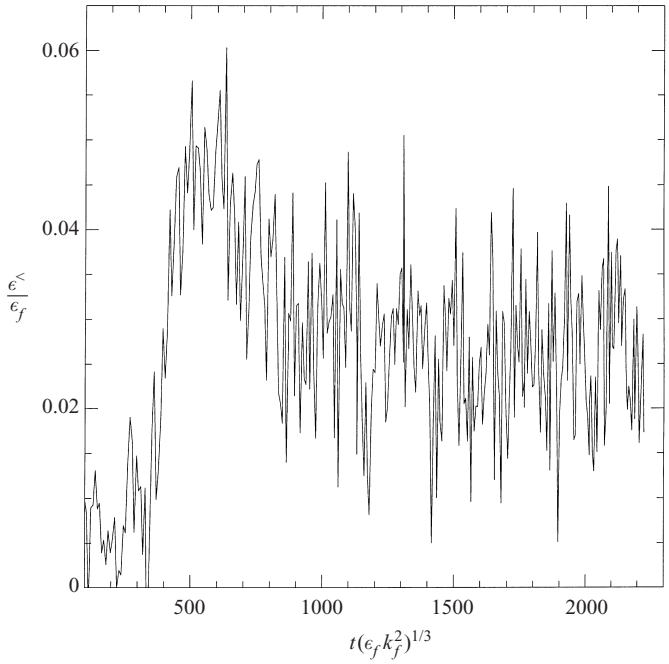

FIGURE 6. Rate of total energy input to scales larger than the forcing scales vs. time for $Fr = 0.21$ and $Ro = 21$ ($N/f = 100$).

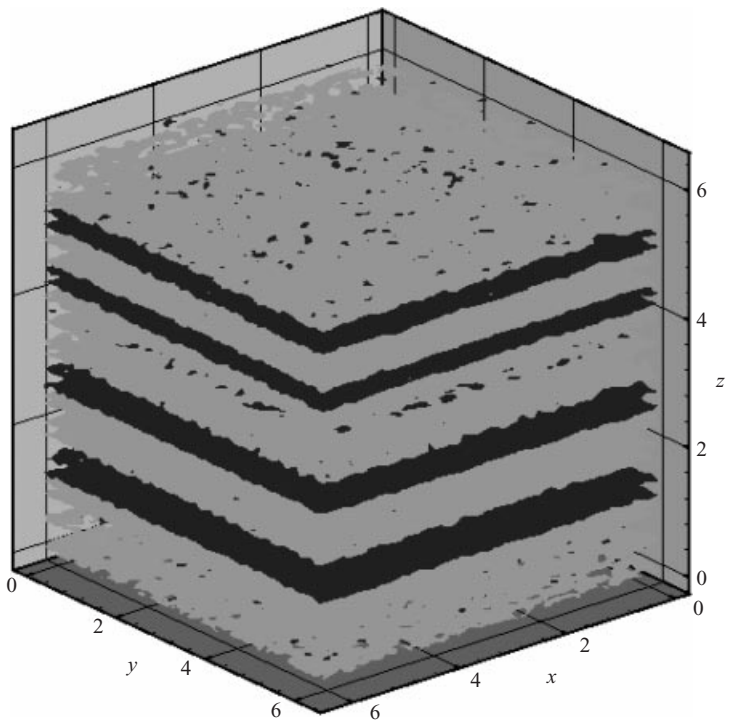

FIGURE 7. Two contour levels of the zonal velocity; $Fr = 0.21$, $Ro = 21$ ($N/f = 100$) and $T \approx 2200$. The dark contours represents positive zonal flow.

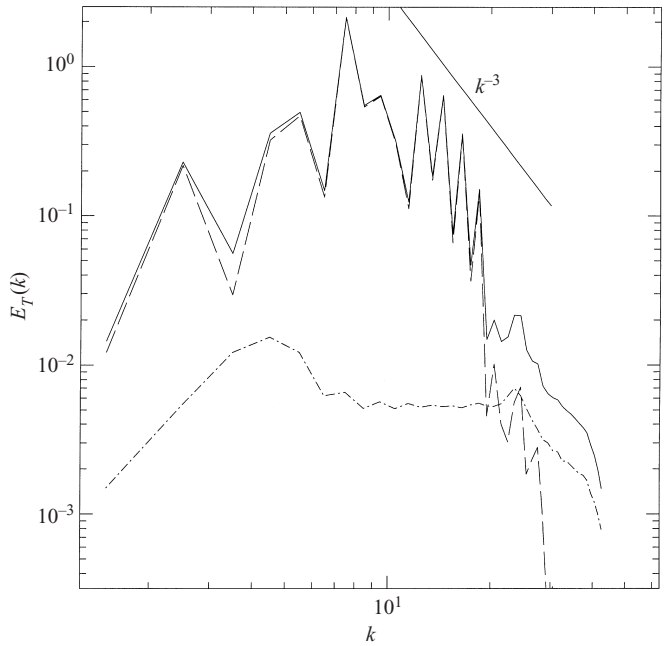

FIGURE 8. Waves only: total energy vs. wavenumber (solid) for $Fr = 0.21$, $Ro = 21$ ($N/f = 100$) and $T \approx 1608$ in a simulation with the PV modes artificially suppressed; total energy in the VSHF modes (2.14) with $\sigma^{\pm} = \pm f$ (long dashes); potential energy of the density fluctuations (dash-dot).

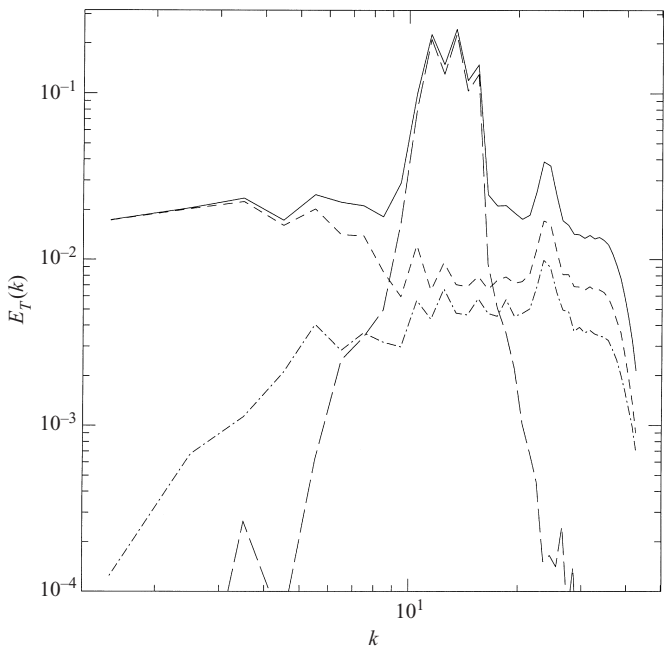

FIGURE 9. Total energy vs. wavenumber (solid) for $Fr = 0.21$, $Ro = 2.1$ ($N/f = 10$) and $T = 605$; total energy in the PV modes (2.13) (short dashes); total energy in the VSHF modes (2.14) with $\sigma^{\pm} = \pm f$ (long dashes); potential energy of the density fluctuations (dash-dot).

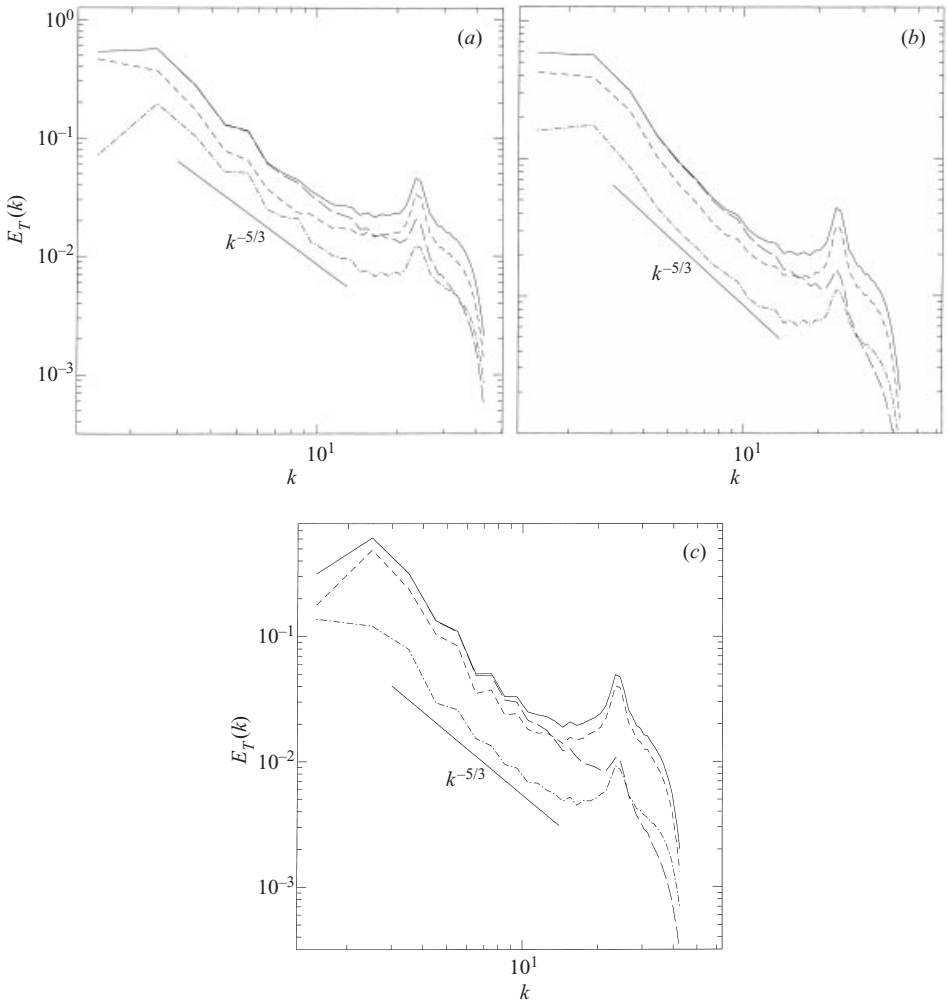

FIGURE 10. Total energy vs. wavenumber (solid) for $Fr = 0.21$, and: (*a*) $Ro = 0.42$ ($N/f = 2$) and $T \approx 170$; (*b*) $Ro = 0.21$ ($N/f = 1$) and $T \approx 120$; (*c*) $Ro = 0.10$ ($N/f = 0.5$) and $T \approx 100$. Total energy in the PV modes (long dashes); kinetic energy (short dashes); potential energy of the density fluctuations (dash-dot).

three-dimensional range of scales, we found an isotropic two-dimensional inverse cascade instead of an anisotropic three-dimensional energy transfer to large scales for $H/L = 1/12$ with resolution $240 \times 240 \times 40$, and also for the larger ratio $H/L = 1/4$ but with lower resolution $128 \times 128 \times 32$ (Smith & Waleffe 1999). Here we performed a simulation with $H/L = 1/2$, $Fr = 0.23$ and $N/f = 100$ such that $NH/(fL) = 50$, with resolution $160 \times 160 \times 80$. The non-dimensional parameter $NH/(fL)$ is the square root of the Burger number. The grid is isotropic at the largest wavenumber (Smith *et al.* 1996), leading to $\Delta k_z \approx 1.6$ and $\Delta k_h \approx 0.8$. With this discretization, and peak forcing wavenumber $k_f \approx 27$, we find essentially the same results as for the unit-aspect-ratio box with $N/f = 100$ (figures 5 and 7), however the growth of the energy is delayed (curve with crosses in figure 4). In the $H/L = 1/2$ case, the energy once again accumulates in the VSHF, primarily in the range $11 \leqslant k \leqslant 12$.

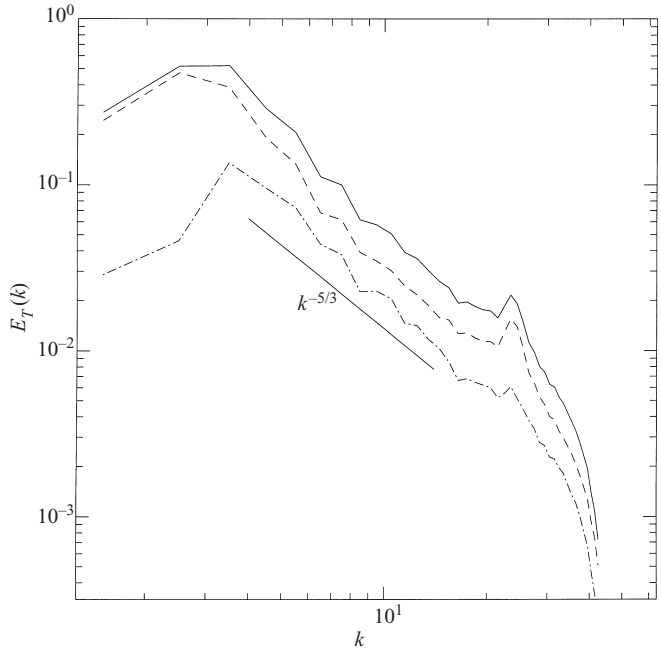

FIGURE 11. PV only: total energy vs. wavenumber (solid) for $Fr = 0.21$, $Ro = 0.42$ ($N/f = 2$) and $T \approx 110$ in quasi-geostrophic turbulence (waves artificially removed); kinetic energy (short dashes); potential energy of the density fluctuations (dash-dot).

5.3. *Decaying for* $H/L = 1$

Although we did not complete a thorough study of decaying turbulence, we did investigate decay for the three cases $Fr = 0.21$ and $N/f = 100$, 1 and $1/2$, starting from the flow fields at the latest times of our forced simulations. Here we used hyperviscosity with $p = 4$ instead of $p = 8$ to accelerate the decay, but still without damping directly the largest scales. For the first case $N/f = 100$, the energy remains in the large-scale VSHF modes for 2000 nonlinear times, without significant change in the structure of the physical-space fields. This is expected as the flow is nearly one-dimensional and there are no nonlinear interactions in a one-dimensional flow, but confirms stability of the flow. For $N/f = 1$, there is an initial period of decay in both the kinetic and potential energies, followed by a period of $O(10^2)$ nonlinear times during which the velocity field gains energy from the density fluctuations such that the kinetic energy grows, even though the total energy decreases. The transfer of kinetic energy to large-scale geostrophic modes continues, and because of the finite box size, kinetic energy begins to accumulate in the geostrophic modes with $k = 1$ (figure 13). The accumulation of energy in $k = 1$ corresponds to the formation of vortical columns (figure 14). The spectrum of the total energy and the spectrum of the geostrophic motions are virtually identical (figure 13), with a power-law scaling somewhat steeper than k^{-3} and more like k^{-4}. Similar results are found for $N/f = 1/2$ ($Fr = 0.21$, $Ro = 0.10$).

6. Summary and discussion

For rotating and stratified flow with $N/f \approx 100$ typical of atmospheric mesoscales, there is conflicting evidence for up-scale energy transfer. As discussed by Lilly

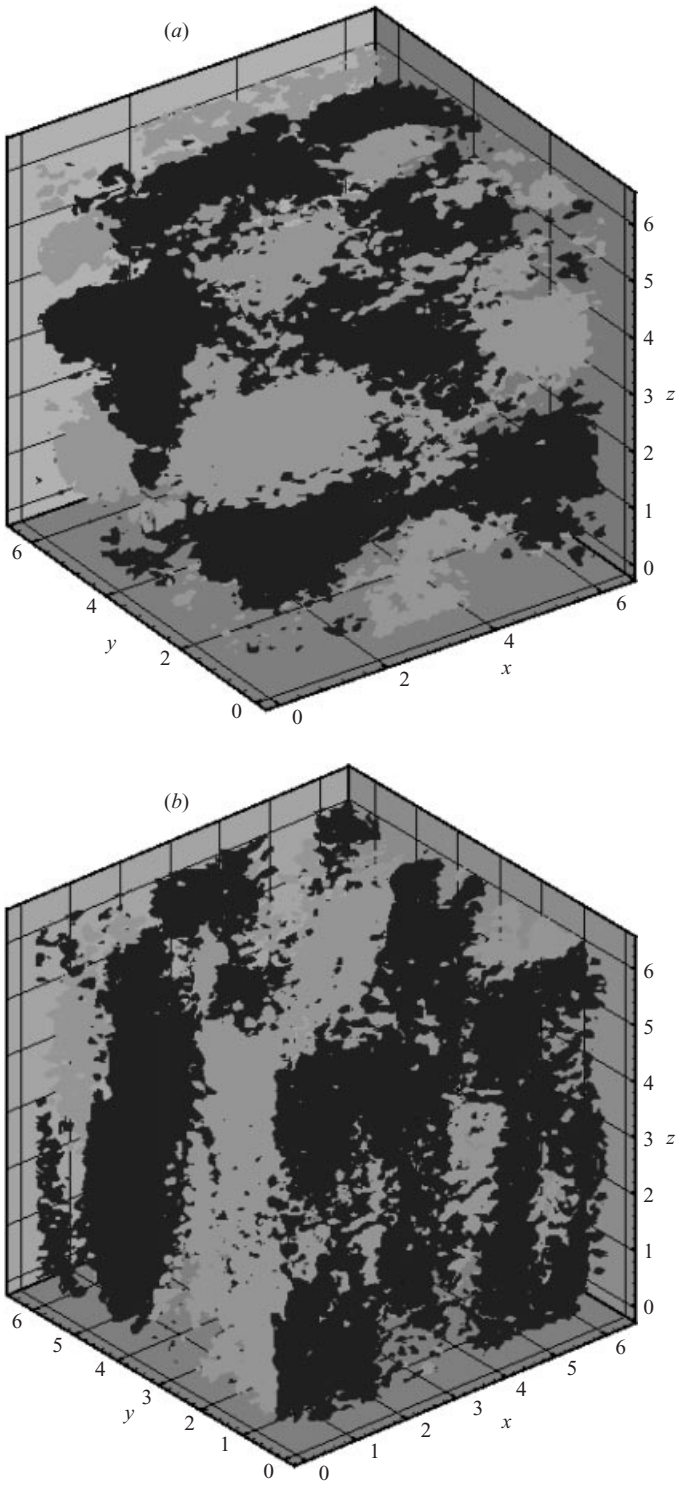

FIGURE 12. Two contour levels of the zonal velocity; $Fr = 0.21$, and (*a*) $Ro = 0.42$ ($N/f = 2$) and $T \approx 170$; (*b*) $Ro = 0.10$ ($N/f = 0.5$) and $T \approx 100$. The dark contours represent positive zonal flow.

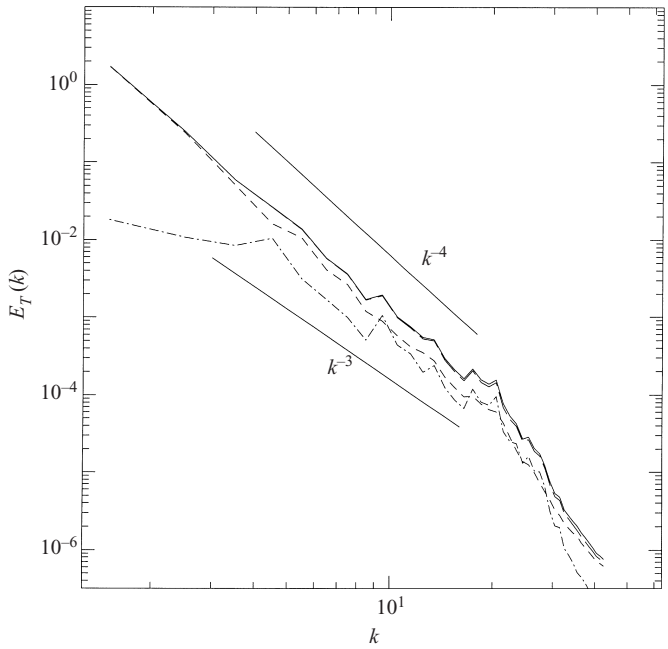

FIGURE 13. Decay: total energy vs. wavenumber (solid) for $Fr = 0.21$, $Ro = 0.21$ ($N/f = 1$) and decay time $T \approx 500$; total energy in the PV modes (2.13) (long dashes); kinetic energy (short dashes); potential energy of the density fluctuations (dash-dot).

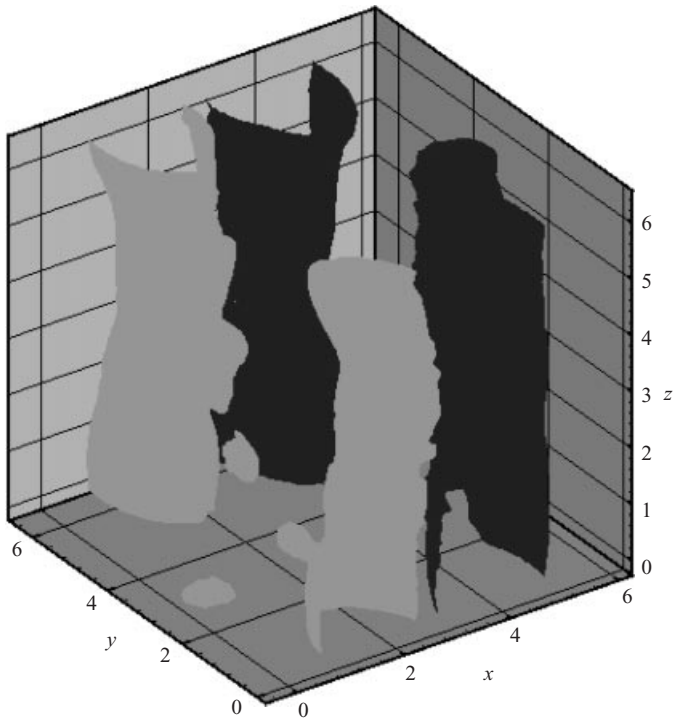

FIGURE 14. Decay: two contour levels of the zonal velocity; $Fr = 0.21$, $Ro = 0.21$ ($N/f = 1$) and decay time $T \approx 500$. The dark contours represent positive zonal flow.

et al. (1998), meteorologically oriented models show isotropic up-scale energy transfer characterized by energy spectrum $E(k) \propto k^{-5/3}$, while previous forced turbulence simulations of the type performed in this work have generally not supported strong up-scale transfer of energy. The presence of the large-scale spectrum $E(k) \propto k^{-5/3}$ in the meteorological models may be partly due to insufficient vertical resolution. Our simulations of rotating flow with low vertical resolution showed a large-scale spectrum close to $E(k) \propto k^{-5/3}$ instead of the long-time scaling $E(k) \propto k^{-3}$ found for increased vertical resolution equal to the horizontal resolution (128^3 Fourier modes) (Smith & Waleffe 1999). Bartello (1998) also finds a large-scale energy spectrum $E(k) \propto k^{-5/3}$ in a calculation with enhanced vertical dissipation. The lack of strong up-scale energy transfer in some turbulence simulations is perhaps due to the combination of increased vertical resolution but insufficient integration time. The present forced turbulence simulations have resolution 128^3 Fourier amplitudes and very long integration times (up to 2200 nonlinear time scales $(\epsilon_f k_f^2)^{-1/3}$ for $N/f = 100$).

For $N/f = 100$, and more generally $N/f \gg 1$, our simulations show an interesting new phenomenon, namely the pile-up of energy in vertically sheared, horizontal motions. A large amount of energy accumulates in selected large scales and there is no power-law scaling of the large-scale energy spectrum. Embid & Majda (1998) emphasize that the slow motions in the low Froude number, finite Rossby number limit ($Fr \to 0$, Ro fixed, hence $N/f = Ro/Fr \to \infty$) consists not only of the three-dimensional horizontal motions $\boldsymbol{v} = \widehat{\boldsymbol{z}} \times \nabla\psi(\boldsymbol{x}, t)$ corresponding to the PV modes (2.13), but also of a vertically sheared, horizontal flow $\boldsymbol{V}_H(z, t)$ corresponding to the VSHF modes (2.14). In the limiting dynamics, both components decouple from the fast inertial–gravity waves but the $\boldsymbol{V}_H(z, t)$ component evolves due to the Coriolis and diffusion terms only (no nonlinear term). Hence the limiting equations do not reveal what, if anything, could generate such motions. However, if the vertically sheared horizontal flow $\boldsymbol{V}_H(z, t)$ is present in the initial conditions then it has a major effect on the dynamics as it shears the PV component of the slow motions, $\widehat{\boldsymbol{z}} \times \nabla\psi(\boldsymbol{x}, t)$. This shearing leads to strong shear-induced diffusion of that component as illustrated by the exact solutions of Majda & Grote (1997). The flow then tends to a layered or 'pancake' structure as opposed to the columnar structures observed in quasi-geostrophic turbulence when $\boldsymbol{V}_H(z, t)$ is absent (McWilliams, Weiss & Yavneh 1994). In this paper, we have shown that the shear flow $\boldsymbol{V}_H(z, t)$ is in fact generated on long time scales from small-scale random forcing for small but finite Froude number and large N/f, namely $Fr = 0.21$, $N/f = 10$, 100 and ∞. Furthermore, our results show that wave interactions are responsible for the generation of the vertically sheared horizontal flow $\boldsymbol{V}_H(z, t)$. The PV modes seem to merely slow down the generation of $\boldsymbol{V}_H(z, t)$ (figure 8). In the opposite limit, $Ro \to 0$, Fr fixed (i.e. $N/f \to 0$), the limiting equations consist of the two-dimensional equations for the z-independent geostrophic flow. For small Ro and $N/f = 0$, our earlier calculations (Smith & Waleffe 1999) did show the analogous generation of large-scale columnar motions, corresponding in fact to cyclonic vortical columns, from small-scale random forcing.

We do not observe the generation of large-scale cyclonic columns or large-scale vertically sheared horizontal flow $\boldsymbol{V}_H(z, t)$ at small Froude and/or Rossby numbers when $1/2 \leqslant N/f \leqslant 2$, although we still observe population of large scales, with the large-scale spectrum scaling approximately like $E(k) \propto k^{-5/3}$. In that range, the PV modes dominate the dynamics. Simulations in which the waves are artificially removed (figure 11) do not show significant differences with the full simulations except that the transfer of energy to large scales by the PV mode interactions is slightly faster. This suggests that the waves are essentially insignificant but have a slight decorrelation

effect on the PV mode interactions, thereby reducing the efficiency of the inverse cascade.

6.1. *Resonant triads*

It is easy to show that the range $1/2 \leqslant N/f \leqslant 2$ is precisely the range where resonant triad interactions of inertial–gravity waves cannot occur. Resonant triad interactions require $\boldsymbol{k}+\boldsymbol{p}+\boldsymbol{q}=0$ and $\sigma(\boldsymbol{k})+\sigma(\boldsymbol{p})+\sigma(\boldsymbol{q})=0$ where the wave frequency σ is given in (2.11). It is clear that if $N=f$ then $\sigma=\pm N$, $\forall \boldsymbol{k}$, and the sum of three frequencies cannot vanish. Indeed, in that case $\sigma(\boldsymbol{k})+\sigma(\boldsymbol{p})+\sigma(\boldsymbol{q}) = \pm N, \pm 2N, \pm 3N$. More generally, (2.11) implies that $\min|\sigma| = \min(N,f)$ and $\max|\sigma| = \max(N,f)$, with these extremas occurring at $k_z=0$ or $k_h=0$. The resonance condition $\sigma(\boldsymbol{k})+\sigma(\boldsymbol{p})+\sigma(\boldsymbol{q})=0$ implies that two of those frequencies must have the same sign while the third has the opposite sign. One can choose $\sigma_1,\sigma_2,\sigma_3 \geqslant 0$ without loss of generality and write the resonance condition as $\sigma_1+\sigma_2=\sigma_3$. This relation can only be satisfied if $2(\min(N,f)) < \max(N,f)$, where we can take the strict inequality because the wavectors must form a triangle and this cannot happen with two horizontal and one vertical wavevectors or vice versa. Hence resonant triads are not possible when

$$\frac{1}{2} \leqslant \frac{N}{f} \leqslant 2. \tag{6.1}$$

Outside but near this range, there are very few resonant triads, if any. Therefore, we expect that resonant triads can play a significant role only if $N/f \ll 1/2$ or $2 \ll N/f$. Our simulations show that the PV modes are insignificant when Fr is small but N/f is large. This suggests that resonant triads, or rather near-resonant triads, of inertial–gravity waves are responsible for the generation of the vertically sheared horizontal flow $\boldsymbol{V}_H(z,t)$ when Fr is smaller than an $O(1)$ critical value and N/f is large, and for the generation of large-scale cyclonic vortices when Ro and N/f are small. This analysis can be extended further. For $N/f < 1/2$, the first resonant triads that come into play consist of one vertical mode $(0,0,k_z)$ (corresponding to the largest $\sigma_3=f$), and two nearly horizontal modes $\boldsymbol{p}$, $\boldsymbol{q}$ with $p_h = q_h \gg |p_z|, |q_z|$ and $|k_z|$ because $k_z+p_z+q_z=0$. The 'instability assumption' (Waleffe 1993) then suggests that, statistically, energy in such a triad will be transferred from the large-scale fast vertical mode to the small-scale slower nearly horizontal modes. Likewise, for $2 < N/f$ the first resonant triads consist of one large-scale fast horizontal mode and two slower, nearly vertical, small-scale modes. One expects transfer from the large-scale fast horizontal mode to the slower small-scale nearly vertical modes in this case. These arguments suggest that the first resonant triad interactions that arise when $N/f < 1/2$ tend to two-dimensionalize the flow (columnar structures), while those that first arise when $2 < N/f$ tend to 'one-dimensionalize' the flow (pancake structures).

6.2. *Quasi-geostrophic equation*

In the range $1/2 \leqslant N/f \leqslant 2$ our forced simulations show that the PV modes strongly dominate at scales larger than the forcing. The large-scale dynamics can thus be seen as resulting from PV mode interactions only. In the absence of forcing and dissipation, those $\boldsymbol{\phi}^0$ interactions are, from (2.13) and (2.18),

$$\frac{\mathrm{d}}{\mathrm{d}t} a^0_{\boldsymbol{k}} = \sum_{\boldsymbol{k}+\boldsymbol{p}+\boldsymbol{q}=0} C_{\boldsymbol{kpq}}\, \overline{a^0_{\boldsymbol{p}}}\, \overline{a^0_{\boldsymbol{q}}}, \tag{6.2}$$

where

$$C_{\boldsymbol{kpq}} = \frac{\mathrm{i}N(\boldsymbol{p}\times\boldsymbol{q}\cdot\widehat{\boldsymbol{z}})}{\sigma_k k\,\sigma_p p\,\sigma_q q}(\sigma_q^2 q^2 - \sigma_p^2 p^2) \tag{6.3}$$

with $\sigma_k k = \left(N^2 k_h^2 + f^2 k_z^2\right)^{1/2}$. The triad constraint $\boldsymbol{k}+\boldsymbol{p}+\boldsymbol{q}=0$ implies that $(\boldsymbol{p}\times\boldsymbol{q}\cdot\widehat{\boldsymbol{z}}) = (\boldsymbol{q}\times\boldsymbol{k}\cdot\widehat{\boldsymbol{z}}) = (\boldsymbol{k}\times\boldsymbol{p}\cdot\widehat{\boldsymbol{z}})$, so $C_{\boldsymbol{kpq}}$ consists of a cyclically symmetric coefficient times $(\sigma_q^2 q^2 - \sigma_p^2 p^2)$. Therefore,

$$C_{\boldsymbol{kpq}} + C_{\boldsymbol{pqk}} + C_{\boldsymbol{qkp}} = 0, \tag{6.4}$$

$$\sigma_k^2 k^2 C_{\boldsymbol{kpq}} + \sigma_p^2 p^2 C_{\boldsymbol{pqk}} + \sigma_q^2 q^2 C_{\boldsymbol{qkp}} = 0, \tag{6.5}$$

and triad interactions have two quadratic invariants: the total energy (kinetic + potential)

$$|a(\boldsymbol{k},t)|^2 + |a(\boldsymbol{p},t)|^2 + |a(\boldsymbol{q},t)|^2 \tag{6.6}$$

and the quadratic part of the potential enstrophy

$$\sigma_k^2 k^2 |a(\boldsymbol{k},t)|^2 + \sigma_p^2 p^2 |a(\boldsymbol{p},t)|^2 + \sigma_q^2 q^2 |a(\boldsymbol{q},t)|^2. \tag{6.7}$$

The equation (6.2) for the PV interactions only can be inverse-Fourier transformed. Letting $\widehat{\psi}_{\boldsymbol{k}} \equiv -Na_{\boldsymbol{k}}^0/(\sigma_k k)$ one can check easily that (6.2), (6.3) is the Fourier transform of

$$\left(\frac{\partial}{\partial t} + \boldsymbol{v}\cdot\nabla\right)\left(\nabla_H^2 + \frac{f^2}{N^2}\frac{\partial^2}{\partial z^2}\right)\psi(\boldsymbol{x},t) = 0, \tag{6.8}$$

where $\nabla_H^2 = \partial^2/\partial x^2 + \partial^2/\partial y^2$ and $\boldsymbol{v} = \widehat{\boldsymbol{z}}\times\nabla\psi$, $\theta = -(f/N)\partial\psi/\partial z$. This is the quasigeostrophic equation† (Charney 1971) which conserves, in particular, the total energy

$$2\frac{\mathrm{d}E}{\mathrm{d}t} \equiv \frac{\mathrm{d}}{\mathrm{d}t}\left\langle\left(\frac{\partial\psi}{\partial x}\right)^2 + \left(\frac{\partial\psi}{\partial y}\right)^2 + \frac{f^2}{N^2}\left(\frac{\partial\psi}{\partial z}\right)^2\right\rangle = 0 \tag{6.9}$$

and the total 'pseudo'-potential enstrophy

$$2\frac{\mathrm{d}F}{\mathrm{d}t} \equiv \frac{\mathrm{d}}{\mathrm{d}t}\left\langle\left(\nabla_H^2\psi + \frac{f^2}{N^2}\frac{\partial^2\psi}{\partial z^2}\right)^2\right\rangle = 0, \tag{6.10}$$

where the angled brackets $\langle\rangle$ denote an integral over the domain. These two quadratic invariants are particularly important because they are the only invariants that are conserved at the level of elementary triad interactions, as shown above (6.3).‡ As Charney (1971) discussed, there is therefore a very close analogy between quasi-geostrophic and two-dimensional turbulence. One can perform the same type of analysis for quasi-geostrophic turbulence as that of Kraichnan (1967) for two-dimensional turbulence, suggesting that forced simulations as performed in this paper would show a $k^{-5/3}$ inverse cascade of energy and a k^{-3} forward cascade of 'pseudo'-potential enstrophy. We do indeed observe a large-scale spectrum $E(k) \propto k^{-5/3}$ when the PV modes dom-

† Salmon (1988, p. 81) discusses a similar 'derivation' of the quasi-geostrophic equation for rotating shallow-water, where resonant triads can never occur (see Embid & Majda 1996 for a rigorous asymptotic derivation).

‡ Conservation of 'pseudo'-potential enstrophy by PV mode interactions is an exact result that can be deduced from conservation of potential enstrophy. No approximation or limiting process (e.g. $Fr \to 0$) is required. However, whether the full dynamics is well approximated by interactions of only the PV modes requires Fr sufficiently small and $1/2 \leqslant N/f \leqslant 2$.

inate, i.e. for Fr smaller than an $O(1)$ critical value but only when $1/2 \leqslant N/f \leqslant 2$. The small-scale spectrum remains dominated by the inertial–gravity waves.

This 'derivation' of the quasi-geostrophic equation appears more restrictive than other derivations as it requires that $1/2 \leqslant N/f \leqslant 2$. However, typical derivations include other assumptions such as strong vertical/horizontal scale disparity ($H \ll L$) and/or hydrostatic equilibrium. Both assumptions have a major impact on resonant wave interactions. When $H \ll L$, the vertical wavenumbers are much sparser than the horizontal wavenumbers, thereby limiting possible (near) resonant interactions. The further delay in the strong growth of the energy in our simulation for $H/L = 1/2$ with respect to the simulation for $H/L = 1$ (figure 4) is consistent with that interpretation. Likewise, the hydrostatic approximation, whose validity requires both $f/N \approx |k_z|/k_h \ll 1$, significantly alters the dispersion relation and thus resonant interactions. In fact, the rotating shallow-water equations have no resonant triads (e.g. Embid & Majda 1996). The recent studies of Embid & Majda (1998) emphasize that asymptotic validity of the quasi-geostrophic equations requires N/f fixed as $Fr \to 0$. Our results suggest the tighter constraint $1/2 \leqslant N/f \leqslant 2$ for small but finite Fr.

7. Conclusions

We have considered the forced, rotating, stably stratified Boussinesq equations. The random forcing is localized at (large) wavenumber k_f and is white-in-time, providing a constant rate of (kinetic) energy input ϵ_f. The Froude and Rossby numbers based on the forcing parameters have the well-defined values $Fr = N^{-1}(\epsilon_f k_f^2)^{1/3}$ and $Ro = f^{-1}(\epsilon_f k_f^2)^{1/3}$, respectively, where N is the buoyancy frequency and f is twice the rotation rate. The numerical results show that when the Froude number is less than an $O(1)$ critical value (≈ 0.5), there is transfer of energy from the small to the large scales. The nature of this transfer depends critically on the ratio N/f. For $2 \ll N/f$, the large scales that arise from the small-scale forcing have the form of a vertically sheared, horizontal flow $\boldsymbol{V}_H(z,t)$ and the PV modes play a secondary, retarding role. For $1/2 \leqslant N/f \leqslant 2$, resonant triads cannot occur and our simulations show that the inertial–gravity waves are insignificant and the dynamics is completely dominated by the PV modes. This is quasi-geostrophic turbulence characterized by the inviscid conservation of two quadratic invariants and a $k^{-5/3}$ inverse energy cascade. Near $N/f \approx 1/2$ the flow shows the development of vortical columns. For $N/f \ll 1/2$, the flow presumably tends to the state observed in our earlier calculations for $Ro \approx 0.1$, $N/f = 0$, where the flow becomes dominated by large-scale *cyclonic* vortices. These results suggest that $1/2 \leqslant N/f \leqslant 2$ is the domain of validity of the quasi-geostrophic model.

Challenges for future research are to understand further the role of resonant triads for $N/f < 1/2$ and $N/f > 2$ and to understand what controls the predominantly cyclonic circulation of the vortical structures when $N/f \to 0$. In addition, it would be interesting to deduce effective asymptotic equations that capture the generation of large scales by wave interactions over long time scales. Most equations are usually deduced from scaling presumptions that filter out the waves at the outset. An exception is the work of Julien, Knobloch & Werne (1998) in rapidly rotating flow ($N = 0$) that includes both geostrophic modes (2.15) and slow inertial waves ((2.12), with $N = 0$, $|k_z| \ll k_h$). As discussed in our earlier work (Waleffe 1993; Smith & Waleffe 1999), resonant interactions can be called upon to transfer energy from fast to slow inertial waves. However, simply including all the resonant interactions in the

asymptotic equations is not computationally effective because of the cost associated with identifying and selecting those interactions.

The authors thank D. Lilly for a thoughtful discussion and probing questions, J. Herring for suggesting the decay runs and G. Vallis for suggesting a run with $H/L < 1$. The authors also thank C. Cambon and the referees for their constructive comments on the manuscript. The support of NSF is gratefully acknowledged, under grants DMS-0071937 (LMS) and DMS-9803685 (FW). Some of the computations were performed on a SGI Origin200 purchased with a NSF SCREMS grant (DMS-9977384). L. M. S. is also grateful for computing resources provided by the National Center for Supercomputing Applications at the University of Illinois.

REFERENCES

Bartello, P. 1995 Geostrophic adjustment and inverse cascades in rotating stratified turbulence. *J. Atmos. Sci.* **52**, 4410–4428.

Bartello, P. 1998 Potential vorticity, resonance and dissipation in rotating, convective turbulence. *Geophysical and Astrophysical Convection* (ed. R. H. Kerr, P. Fox & C.-H. Moeng). Gordon and Breach.

Cambon, C. 2001 Turbulence and vortex structures in rotating and stratified flows. *Eur. J. Mech.* B **4**, 489–510.

Canuto, C., Hussaini, M. Y., Quarteroni, A. & Zang, T. A. 1988 *Spectral Methods in Fluid Dynamics*. Springer.

Charney, J. G. 1971 Geostrophic turbulence. *J. Atmos. Sci.* **28**, 1087–1095.

Chasnov, J. R. 1994 Similarity states of passive scalar transport in isotropic turbulence. *Phys. Fluids* **6**, 1036–1051.

Chekhlov, A., Orszag, S. A., Sukoriansky, S., Galperin, B. & Staroselsky, I. 1996 The effect of small-scale forcing on large-scale structures in two-dimensional flows. *Physica* D **98**, 321–334.

Embid, P. & Majda, A. J. 1996 Averaging over fast gravity waves for geophysical flows with arbitrary potential vorticity. *Commun. Partial Difft Equat.* **21**, 619–658.

Embid, P. & Majda, A. J. 1998 Low froude number limiting dynamics for stably stratified flow with small or finite Rossby numbers. *Geophys. Astrophys. Fluid Dyn.* **87**, 1–50.

Gage, K. S. & Nastrom, G. D. 1986 Theoretical interpretation of atmospheric wavenumber spectra of wind and temperature observed by commercial aircraft during GASP. *J. Atmos. Sci.* **43**, 729–740.

Godeferd, F. S. & Cambon, C. 1994 Detailed investigation of energy transfers in homogeneous stratified turbulence. *Phys. Fluids* **6**, 2084–2100.

Greenspan, H. P. 1969 On the nonlinear interaction of inertial modes. *J. Fluid Mech.* **36**, 257–264.

Hasselman, K. 1976 Stochastic climate models. *Tellus* **28**, 473–485.

Herring, J. R. & Metais, O. 1989 Numerical experiments in forced stably stratified turbulence. *J. Fluid Mech.* **202**, 97–115.

Huang, H.-P., Galperin, B. & Sukoriansky, S. 2000 Anisotropic spectra in two-dimensional turbulence on the surface of a sphere. *Phys. Fluids* **13**, 225–240.

Julien, K., Knobloch, E. & Werne, J. 1998 A new class of equations for rotationally constrained flows. *Theoret. Comput. Fluid Dyn.* **11**, 251–261.

Kraichnan, R. H. 1967 Inertial ranges in two-dimensional turbulence. *Phys. Fluids* **10**, 1417–1423.

Lelong, P. & Riley, J. J. 1991 Internal wave-vortical mode interactions in strongly stratified flows. *J. Fluid Mech.* **232**, 1–19.

Lilly, D. K. 1983 Stratified turbulence and mesoscale variability in the atmosphere. *J. Atmos. Sci.* **40**, 749–761.

Lilly, D. K. 1989 Two-dimensional turbulence generated by energy sources at two scales. *J. Atmos. Sci.* **46**, 2026–2030.

Lilly, D. K., Bassett, G., Droegemeier, K. & Bartello, P. 1998 Stratified Turbulence in the Atmospheric Mesoscales. *Theoret. Comput. Fluid Dyn.* **11**, 139–153.

Longuet-Higgins, M. S. & Gill, A. E. 1967 Resonant interactions between planetary waves. *Proc. R. Soc. Lond.* A **299**, 120–140.

Majda, A. J. & Embid, P. 1998 Averaging over fast gravity waves for geophysical flows with unbalanced initial data. *Theoret. Comput. Fluid Dyn.* **11**, 155–169.

Majda, A. J. & Grote, M. J. 1997 Model dynamics and vertical collapse in decaying strongly stratified flows. *Phys. Fluids* **9**, 2932–2940.

Majda, A. J., Timofeyev, I. & Vanden Eijnden, E. 1999 Models for stochastic climate prediction. *Proc. Natl Acad. Sci.* **96**, 14687–14691.

Maltrud, M. E. & Vallis, G. K. 1991 Energy spectra and coherent vortices in force two-dimensional and β-plane turbulence. *J. Fluid Mech.* **228**, 321–342.

McWilliams, J. C., Weiss, J. B. & Yavneh, I. 1994 Anisotropy and coherent vortex structures in planetary turbulence. *Science* **264**, 410–413.

Metais, O., Bartello, P., Garnier, E., Riley, J. J. & Lesieur, M. 1996 Inverse cascade in stably stratified rotating turbulence. *Dyn. Atmos. Oceans* **23**, 193–203.

Nastrom, G. D. & Gage, K. S. 1985 A climatology of aircraft wavenumber spectra observed by commercial aircraft. *J. Atmos. Sci.* **42**, 950–960.

Paret, J. & Tabeling, P. 1998 Intermittency in the two-dimensional inverse cascade of energy: experimental observations. *Phys. Fluids* **10**, 3126–3136.

Phillips, O. M. 1968 The interaction trapping of internal gravity waves. *J. Fluid Mech.* **34**, 407–416.

Riley, J. J. & Lelong, M. P. 2000 Fluid motions in the presence of strong stable stratification. *Annu. Rev. Fluid Mech.* **32**, 613–665.

Rogallo, R. S. 1981 Numerical experiments in homogeneous turbulence. *NASA Tech. Mem.* 81835.

Salmon, R. 1998 *Lectures on Geophysical Fluid Dynamics*. Oxford University Press.

Smith, L. M. 2001 Numerical study of two-dimensional stratified turbulence. In *Advances in Wave Interaction and Turbulence* (ed. P. A. Milewski, L. M. Smith, F. Waleffe & E. G. Tabak). Amer. Math. Soc., Providence, RI.

Smith, L. M., Chasnov, J. & Waleffe, F. 1996 Crossover from two- to three-dimensional turbulence. *Phys. Rev. Lett.* **77**, 2467–2470.

Smith, L. M. & Waleffe, F. 1999 Transfer of energy to two-dimensional large scales in forced, rotating three-dimensional turbulence. *Phys. Fluids* **11**, 1608–1622.

Smith, L. M. & Yakhot, V. 1994 Finite-size effects in forced two-dimensional turbulence. *J. Fluid Mech.* **274**, 115–138.

Staquet, C. & Godeferd, F. S. 1998 Statistical modelling and direct numerical simulations of decaying stably stratified turbulence. Part 1. Flow energetics. *J. Fluid Mech.* **360**, 295–340.

Vincent, D. G. & Schlatter, T. W. 1979 Evidence of deep convection as a source of synoptic-scale kinetic energy. *Tellus* **31**, 493–504.

Waleffe, F. 1993 Inertial transfers in the helical decomposition. *Phys. Fluids* A **5**, 677–685.

Warn, T. 1986 Statistical mechanical equilibria of the shallow water equations. *Tellus* **38A**, 1–11.